crystals

MDPI

Article

Studies on Optoelectronic and Transport Properties of $XSnBr_3$ (X = Rb/Cs): A DFT Insight

Debidatta Behera [1], Boumaza Akila [2], Sanat Kumar Mukherjee [1,*], Tesfaye Abebe Geleta [3,4], Ahmed Shaker [5] and Mostafa M. Salah [6,*]

1 Department of Physics, Birla Institute of Technology, Mesra, Ranchi 835215, India; debidatta95@yahoo.com
2 Radiation Physics Laboratory (LPR), Department of Physics, Faculty of Sciences, Badji Mokhtar University, BP 12, Annaba 23000, Algeria; boumaza.akila@yahoo.fr
3 Graduate Institute of Applied Science and Technology, National Taiwan University of Science and Technology, Taipei 10607, Taiwan; tesfayea867@gmail.com
4 MacDermid Alpha Electronics Solutions Company, Taoyuan 32062, Taiwan
5 Engineering Physics and Mathematics Department, Faculty of Engineering, Ain Shams University, Cairo 11517, Egypt; ahmed.shaker@eng.asu.edu.eg
6 Electrical Engineering Department, Future University in Egypt, Cairo 11835, Egypt
* Correspondence: sanat_aphy@yahoo.co.in (S.K.M.); mostafa.abdulkhalek@fue.edu.eg (M.M.S.)

Abstract: Modern manufacturing is aiming for products that are readily available, environmentally sustainable, and energy efficient. This paper delves into the exploration of compounds meeting these criteria. Specifically, we investigate the structural, elastic, optoelectronic, and transport properties of $XSnBr_3$ (X = Rb/Cs) compounds utilizing the full-potential linearized augmented plane wave program (FP LAPW), a component of Wien2K software. Structural optimization is carried out through the generalized gradient approximation (GGA) approach, yielding lattice constants consistent with preceding numerical and experimental studies. The explored $XSnBr_3$ (X = Rb/Cs) materials exhibit ductility and mechanical stability. Notably, $XSnBr_3$ (X = Rb/Cs) displays a direct bandgap, signifying its semiconducting nature. The bandgap values, as determined by the modified Becke–Johnson (mBJ) approach, stand at 2.07 eV for X = Rb and 2.14 eV for $XSnBr_3$ (X = Rb/Cs). Furthermore, utilizing the BoltzTraP software's transport feature, we investigate thermoelectric properties. Remarkably, $XSnBr_3$ (X = Rb/Cs) demonstrates impressive figures of merit (ZT) at room temperature, implying its potential to serve as a material for highly efficient thermoelectric devices. This research holds promise for contributing to the development of environmentally friendly and energy-efficient technologies.

Keywords: density functional theory (DFT); perovskites; Poisson ratio; optical properties; thermoelectric

Citation: Behera, D.; Akila, B.; Mukherjee, S.K.; Geleta, T.A.; Shaker, A.; Salah, M.M. Studies on Optoelectronic and Transport Properties of $XSnBr_3$ (X = Rb/Cs): A DFT Insight. *Crystals* **2023**, *13*, 1437. https://doi.org/10.3390/cryst13101437

Academic Editors: Sawanta S. Mali and Xiaoping Wang

Received: 1 September 2023
Revised: 13 September 2023
Accepted: 23 September 2023
Published: 27 September 2023

1. Introduction

Globally, there is a rapid increase in the consumption of fossil fuels, leading to detrimental environmental impacts and the exacerbation of global warming. Due to the high cost and potential environmental hazards associated with petroleum usage, exploring alternative energy sources is crucial. To address the challenges posed by global warming, the excessive dependence on fossil fuels, and the utilization of waste heat from vehicles and industrial machinery, researchers in the field of material science are placing greater emphasis on investigating the thermoelectric properties of various alloys and compounds [1–5]. The conversion of waste heat into energy helps alleviate the demand for fossil fuels and mitigates its environmental impact. The dimensionless figure of merit, $ZT = S^2\sigma T/\kappa$, serves as a crucial indicator of the efficiency of thermoelectric materials. This value is determined by several key thermoelectric properties, including the Seebeck coefficient (S), which quantifies the voltage generated from a temperature gradient, the electrical conductivity (σ/τ) denoting the material's ability to carry electrical current, and the thermal conductivity (κ/τ), which characterizes its capacity to conduct heat. In essence, ZT encapsulates the balance

between the material's ability to generate an electric potential difference from temperature variations and its capacity to maintain this difference against heat dissipation. Thus, higher ZT values correspond to superior thermoelectric materials that efficiently convert heat into electricity [6–8]. ZT optimization is challenging because the factors that affect ZT are inversely correlated. Discovering novel compounds with high ZT values is challenging because of the tight interdependence among all three factors: electrical structure, charge carrier concentration, and crystalline structure. Although there are several theoretical models for improving material efficiency, nanostructured engineering and the usage of superlattice or quantum well structures are the ones that have the most success [9].

Due to the adverse consequences of climate change on the environment, there has been a noticeable rise in research on materials and chemicals relevant to optoelectronic and energy conversion applications in recent decades. Numerous inorganic and organic halide perovskite materials have demonstrated excellent application potential as solar materials due to their exceptional productivity in power transformation, high carrier mobility, and other beneficial properties [10–12]. They have been found to have excellent applications in electrical, optoelectronic, and thermoelectric transmission. One of the most significant perovskites is the organic–inorganic hybrid $CH_3NH_3PbI_3$, which has wide absorption, high mobility, and other advantageous thermoelectric and optoelectronic properties [13–15]. There have been a few notable constraints, such as lead's growing toxicity, which is unfavorable because of environmental considerations. Additionally, it has been shown that the organic component degrades and generates harmful compounds when used with inorganic and organic–inorganic hybrid compounds to replace the Pb atom, as well as perovskite compounds with equivalent oxidation states and lead-free replacement metal atoms [16,17]. These substitutions nonetheless demonstrate that lead-free compounds have a lower ZT, and they are only slightly more favorable for changing energy, necessitating more research in halide-based perovskite compounds.

Despite the fact that the organic component of hybrid perovskites degrades at high temperatures, inorganic halide perovskite compounds have been the subject of substantial research [18,19]. These studies are being carried out on compounds with different architectural arrangements, with the main focus being on the features of the compounds employing computer programs. They have the generic formula ABX_3, where X is a halide (Cl, Br, or I atoms), and A and B are elements from the main group [20,21]. The significance of halide perovskites with a chemical composition of ABX_3 has grown in a number of research domains because of their adaptive and highly beneficial physical characteristics in areas like photovoltaics, piezoelectricity, and optoelectronics. According to a thorough assessment of the literature, perovskites with good optoelectronic and transport capabilities include $SrTiO_3$, $XFeO_3$ (X = Ag, Zr), and $LaAlO_3$ [22–24]. Additionally, Bouadjemi investigated the magnetic and physical characteristics of $NdMnO_3$ using density functional theory (DFT) [25]. A new material for optical LEO operation is $BaThO_3$ [26]. Due to the characteristics of $BiBO_3$ and $BiAlO_3$, optoelectronic devices can gain from reduced UV area, visibility, and invisibility [27]. $CsPbX_3$ (X = Cl, Br, and I)'s electrical, optical, and physical properties have been discussed [28]. The Cs base material $CsMO_3$ (M = Ta, Nb)'s mechanical, optical, and thermodynamic properties have been identified [29]. The lattice alteration of Cs-based $CsPbX_3$ has allowed for computational analysis of the bandgap change. The physical properties of cubic perovskite oxides need to be confirmed, according to previous investigations [23].

As was already noted, Cs-based halide perovskites have been researched and are well known; however, as of now, not much is known about $CsXO_3$ (X = Ge, Sn, Pb) [30]. The chemical and physical characteristics of numerous appliances can be enhanced by switching the B site in transition metals. In order to replace lead, scientists have tried using a metal from group 14 of the periodic table, such as Sn or Ge. In this paper, first-principles computations are utilized to compare the electronic, optical, and thermoelectric attributes of perovskite Sn-halide materials $XSnBr_3$ (X = Rb/Cs). These perovskites may be employed in nano-optoelectronic devices, according to studies of their optical characteristics. The

subsequent sections of this paper are organized as follows to provide a comprehensive exploration of the subject matter. Section 2 delves into the intricacies of the computational methodologies employed in this study, outlining the specific techniques and tools used to conduct our analyses. In Sections 3 and 4, we extensively discuss and present the outcomes of our research. These sections offer a detailed breakdown of our findings, addressing each aspect of our investigation and drawing meaningful conclusions from our results.

2. Computational Method

The first-principles computations in the present investigation were performed using the full plane wave augmented plane wave technique [31] implementation of the WIEN2k package [32]. The generalized gradient approximation (GGA) [33], and the preferred modified Becke–Johnson (mBJ) approach [34] which is used to properly anticipate band structure computations, were utilized to explain the electronic exchange and correlation potentials. The bandgap underestimate that existed in earlier classical LDA and GGA techniques is addressed in this upgrade. The l_{max} value was set to 10. To calculate a converged scf, we utilized cut off energy = −6.0 Ry, $R_{MT}K_{Max}$ = 7, and k-points = 10,000 [35]. A 21 × 21 × 21 k-mesh has been used to incorporate the Brillouin zone into the Monkhorst–Pack design. The thermoelectric properties were calculated using the BoltzTraP technique [36]. We sampled the Brillouin Zone of a 46 × 46 × 46 k-mesh, a denser mesh, to obtain more accurate findings.

3. Results and Discussion

3.1. Structural Properties

As previously noted, we improved the topologies of the under-researched compounds while taking into account their cubic structure. Figure 1 depicts their fully relaxed structure. In contrast to the ion Cs/Rb, which is placed at (0,0,0), the component atoms Ge and Br are situated at (1/2,1/2,1/2) and (1/2,1/2,0), respectively [37]. It is found that the studied compounds have a cubic Pm3m space group. To obtain the ideal lattice parameters, as illustrated in Figure 2, the Birch–Murnaghan equation of state against volume (a.u.) [38] and the PBE-GGA functional were utilized, demonstrating that when the atomic number increases, the lattice characteristics improve. From Rb to Cs, the atomic radius increases, changing the ionic bond strength, which mostly impacts the strength of the ionic bonds. The magnitudes of the lattice parameters (a_0), bulk modulus (B), and its pressure derivative (B_p) were determined and depicted in Table 1 and found to be in good agreement with earlier reports. The equilibrium energies of the investigated compounds are found to be negative, which suggests their stability. The bulk modulus is found to decrease from $RbSnBr_3$ to $CsSnBr_3$, which arises because of the interaction of halide ions with Rb/Cs atoms. This again signifies that the compressibility of these compounds raises while their stiffness is reduced as we proceed from $RbSnBr_3$ to $CsSnBr_3$. Additionally, the tolerance factor (τ) was devised to account for the cubic structural features [39]. The examined compound is assumed to have a cubic structure if the indicator parameter's value falls within the range of 0.95 and 1.04. Table 1 displays the predicted value of the τ, which represents the cubic structure. Additionally, the thermodynamic stability can be affected by taking the Formation energy (E_f) into account [40,41]. Table 1 displays the predicted E_f for $XSnBr_3$ (X = Rb/Cs). Thermodynamic stability is demonstrated by the negative formation energy.

3.2. Elastic Characteristics

Hardness, stress, and other structural deformations caused by pressure have all been studied using the elastic constant. The study of these constants is very helpful for understanding the Poisson ratio effect, Young's modulus, Debye temperature, and melting temperature, among other topics. There are three diverse elastic components for cubic crystals: C_{11}, C_{12}, as well as C_{44} [43]. The elastic constant tensors, or C_{ij} in Voigt notation, have emerged as a result of the shift in internal energy deformation in this instance. By

expanding the elastic energy or stress relative to the applied strain, Taylor's formula defines elastic tensors of any order. To define the dynamic and mechanical behavior of the alloys under study, the three second-order elastic coefficients (SOECs) C_{11}, C_{12}, and C_{44} must be determined. The only three distinct elastic constants for cubic crystal formations, according to Hooke's law, are C_{11}, C_{12}, and C_{44}. We may infer that $C_{11} = C_{22} = C_{33}$, $C_{12} = C_{13} = C_{23}$, and $C_{44} = C_{55} = C_{66}$ from the symmetry of the second-order elastic constant matrix. All of the eigenvalues of the elastic constant matrix are non-zero, supporting the stability of the compound. The Born-theory-based stability criteria are presented below in addition to this condition.

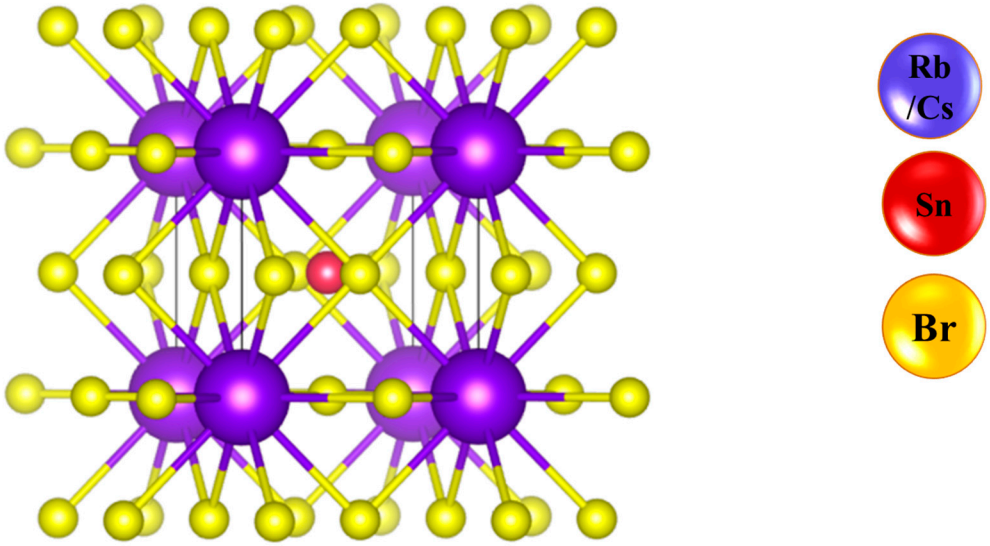

Figure 1. Crystal structure for the studied cubic perovskites $XSnBr_3$ (X = Rb/Cs).

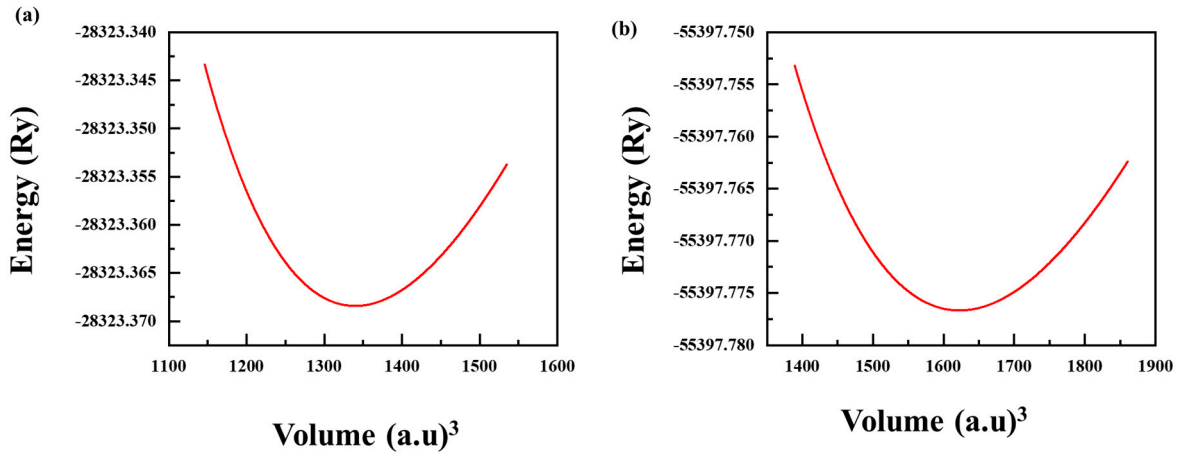

Figure 2. Total energy with volume optimization curves for (**a**) $RbSnBr_3$ and (**b**) $CsSnBr_3$.

Table 1. The evaluated lattice constant a (Å), bulk modulus **B** (GPa), derivative of the bulk modulus B_p, tolerance factor (τ) as well as formation energy (E_f) for $XSnBr_3$ (X = Rb/Cs).

HH	a (Å)	V (a.u.)^3	B	B_p	E_{tot} (Ry)	τ	E_f (eV/atom)
$RbSnBr_3$	5.61	545.005	43.869	3.935	−7676.422	0.97	−1.662
$CsSnBr_3$	5.82	651.515	35.041	4.014	−19,454.663	0.96	−1.690
Other Studies [42]	5.46						

$C_{11} > |C_{12}|$, $C_{11} > 0$, and $(C_{11} + 2C_{12}) > 0$ are all greater than zero [44]. Since it is expected that cubic crystals' elastic constants are compatible with the aforementioned stability conditions, the studied $XSnBr_3$ (X = Rb/Cs) compounds are mechanically stable. The bulk modulus (B), a metric of compressibility resistance, specifies the solid's resistance to volume change, whereas the shear modulus specifies the solid's resistance to shear deformation while preserving volume [45]. Elastic structures play a significant role in the analysis and construction of materials. The computed outcomes are discovered to be consistent with past studies, as shown in Table 2. The bulk modulus has been calculated using the formula $B = C_{11} + 2C_{12}/3$. The good value of B is used to estimate the good crystal strength of the $XSnBr_3$ (X = Rb/Cs). The significant value of G, as shown in Table 2, supports their ability to subsequently flex transversely [46,47]. Young's modulus (E) and Poisson's ratio (σ) are calculated using the following formulas, $\sigma = 3B\ 0–E/6B$ and $E = 9BG/3B + G$. Table 2 displays the expected values for E and σ. These cubic crystals' anisotropy is measured by Zener's anisotropy index (A) [48,49], which has the formula $A = 2C_{44}/C_{11}–C_{12}$. In some circumstances, the amount of elastic anisotropy (A) is helpful. If A is zero or one, the crystal represents elastic isotropy; otherwise, it represents the proportional degree of elastic anisotropy that the crystal truly contains. As a result, Table 2 interferes with the anisotropic nature of the $XSnBr_3$ (X = Rb/Cs). Additionally, the computed Pugh ratio (B/G) [50] and Poisson ratio interact with the examined $XSnBr_3$ (X = Rb/Cs) compounds' ductility. We estimated the wave velocities V_S, V_P, and V_m from the data on the elastic characteristics of the materials and acquired them from the Navier equation shown below and summarized in Table 2.

Table 2. Computed elastic properties of $XSnBr_3$ (X = Rb/Cs) using GGA-PBE exchange correlation functionals.

Material Property	$RbSnBr_3$	$CsSnBr_3$	Other Studies [42]
C_{11} (GPa)	61.93	63.88	58.18
C_{12} (GPa)	10.83	12.32	11.70
C_{44} (GPa)	7.62	7.14	9.27
S_{11} (GPa^{-1})	0.01710179	0.01669554	
S_{12} (GPa^{-1})	−0.00246767	−0.00269933	
S_{44} (GPa^{-1})	0.13123359	0.14005602	
Bulk modulus, B (GPa)	27.87	29.51	27.00
Shear modulus, G (GPa)	14.79	14.59	13.53
Young modulus, E (GPa)	37.70	37.58	34.83
Poisson ratio, σ (GPa)	0.27	0.28	
Pugh ratio, B/G (GPa)	1.88	2.02	2.01
Cauchy pressure C^P (GPa)	3.21	5.18	
Anisotropy factor (A)	0.29	0.27	
Transverse sound velocity (m/s)	1706	16,585	
Longitudinal sound velocity(m/s)	3204	3254	
Average sound velocity (m/s)	1906	1886	
Temperature Θ_D (K)	199	196.6	
Melting temperature T_m(K)	783.7	768	

$$V_s = \left[\frac{G_H}{\rho}\right]^{1/2}; V_s = \left[\frac{B_{H+}4/3G_H}{\rho}\right]^{1/2}; \; V_m = \left[\frac{\frac{2}{V_S^3} + \frac{1}{V_P^3}}{3}\right]^{-1/3} \quad (1)$$

Another method to calculate Debye temperature is to estimate it from average elastic wave velocity V_m, represented as

$$\theta_D = \frac{h}{k}\left[\frac{3n}{4\pi}\left(\frac{N_A\rho}{M}\right)\right]^{1/3} V_m \quad (2)$$

Here, h, k, N_A, are Planck's constant, Boltzmann's constant, Avogadro's number, respectively, while n and M are the number of atoms per formula unit and molecular mass per formula unit, respectively. The density of the compound is $\rho = M/V$. All computed values are represented in Table 2.

The analysis of the elastic properties of three-dimensional (3D) surfaces helps to visualize and completely explain the anisotropic behavior of the mechanical modulus as represented in Figures 3 and 4 [51]. The Bulk modulus B, Young's modulus E, and shear modulus G's dependency on crystallographic direction can be calculated using the formulas below:

$$\begin{aligned} \tfrac{1}{B} = (S_{11} + 2S_{12}) \quad & \left(l_1^2 + l_2^2 + l_3^2\right) \quad \tfrac{1}{E} \\ & = S_{11} - 2\left(S_{11} - S_{12} - \tfrac{1}{2}S_{44}\right)\left(l_1^2 l_2^2 + l_2^2 l_3^2 + l_3^2 l_1^2\right) \end{aligned} \quad (3)$$

$$\frac{1}{G} = S_{44} - 4\left(S_{11} - S_{12} - \frac{1}{2}S_{44}\right)\left(sin^2\theta.cos^2\theta + 0.125sin^4\right)(1 - cos4\varphi) \quad (4)$$

S_{ij} are the contents of the elastic compliance constants' matrix, which are acquired from the inverse of the elastic constant's matrix $S_{ij} = C_{ij}^{-1}$ and their values are represented in matrix form below. l_1, l_2, and l_3 are the x, y and z-axis director cosines, respectively.

$$S_{ij} = \begin{pmatrix} S_{11} & S_{12} & S_{12} & 0 & 0 & 0 \\ S_{12} & S_{11} & S_{12} & 0 & 0 & 0 \\ S_{12} & S_{12} & S_{11} & 0 & 0 & 0 \\ 0 & 0 & 0 & S_{44} & 0 & 0 \\ 0 & 0 & 0 & 0 & S_{44} & 0 \\ 0 & 0 & 0 & 0 & 0 & S_{44} \end{pmatrix} \quad (5)$$

The degree of divergence from a spherical form often represents the degree of anisotropy. The linear compressibility obtained 3D directional dependency and cross-section in many reticular planes. The fact that Y and G greatly diverge from the sphere and confirm the large anisotropy of $XSnBr_3$ (X = Rb/Cs) supports the spherical shape of the linear compressibility. Furthermore, it is clear from Figure 3 that for both compounds under investigation, the stress along the [100], [010], and [001] axes results in the highest Young modulus value. Conversely, the maximum shear modulus value is obtained when external force is applied along the [111] direction, demonstrating both strong stiffness and weak shear deformation resistance along the [100], [010], and [001] directions.

3.3. Electronic Properties

The predicted results for the band structure are displayed in Figure 5, which demonstrate the presence of the E_F valence band VB below the Fermi energy. The bandgap is calculated taking into account a number of approximations, including GGA-PBE and mBJ. In comparison to alternative approximations, the computed bandgap taking into account mBJ is found to be 2.07 eV and 2.14 eV higher and can therefore be taken as being equivalent to the experimental value.

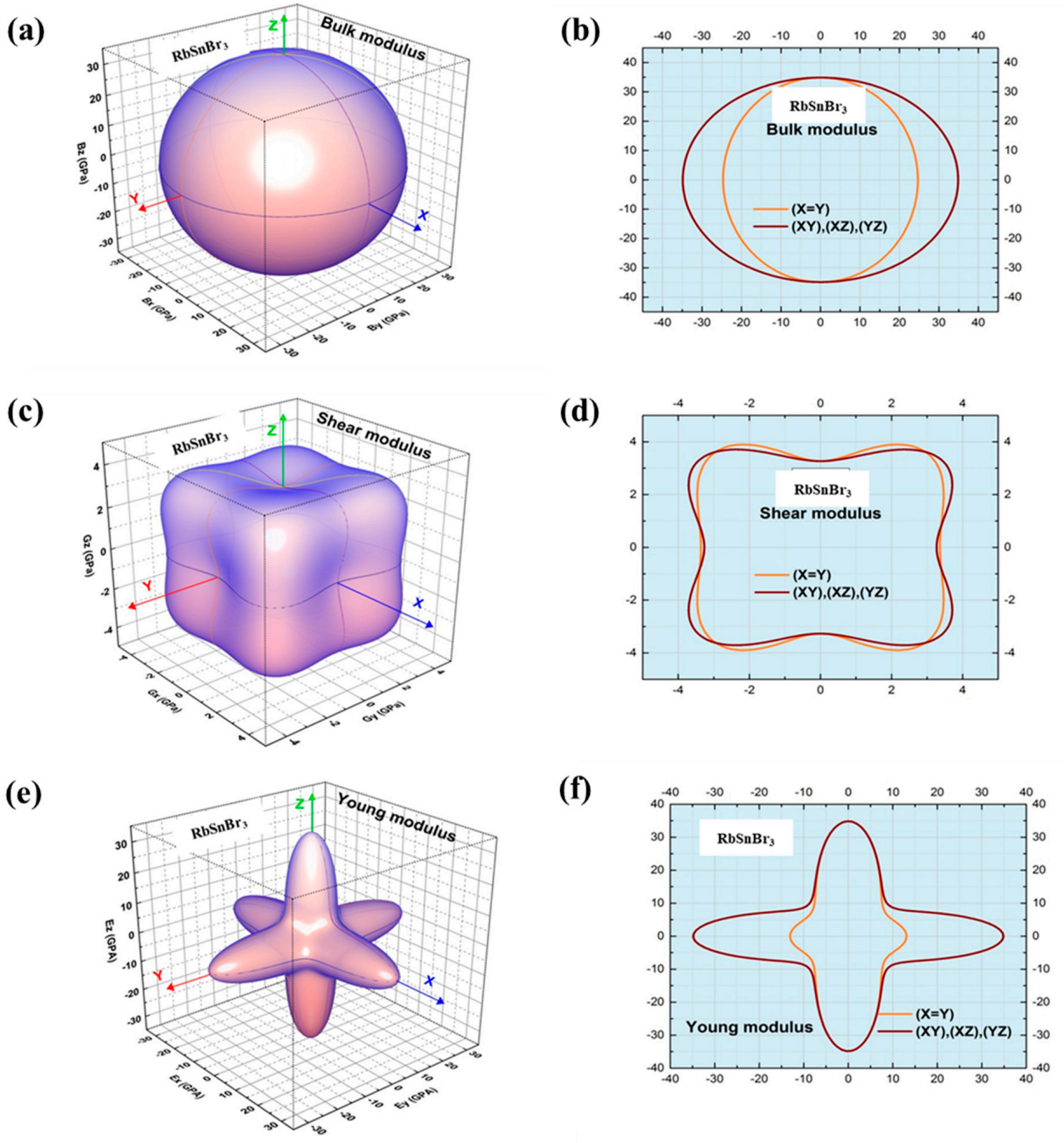

Figure 3. (**a**,**b**) 3D representations of the crystal direction dependency of the Bulk modulus (*B*, in GPa), (**c**,**d**) shear modulus *G* and (**e**,**f**) Young Modulus (*Y*) for $RbSnBr_3$.

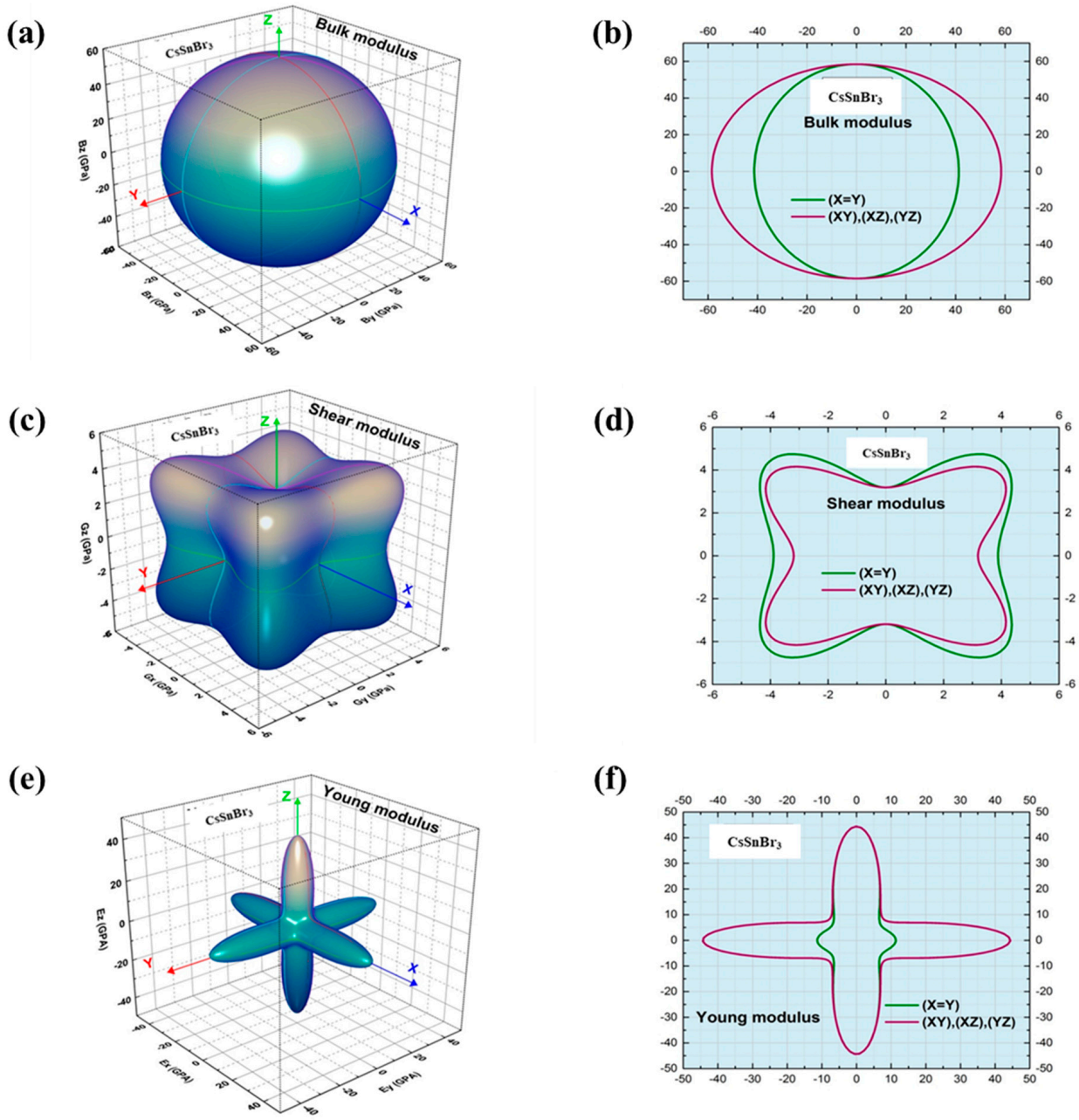

Figure 4. (**a**,**b**) 3D representations of the crystal direction dependency of the Bulk modulus (*B*, in GPa), (**c**,**d**) shear modulus G and (**e**,**f**) Young Modulus (*Y*) for $CsSnBr_3$.

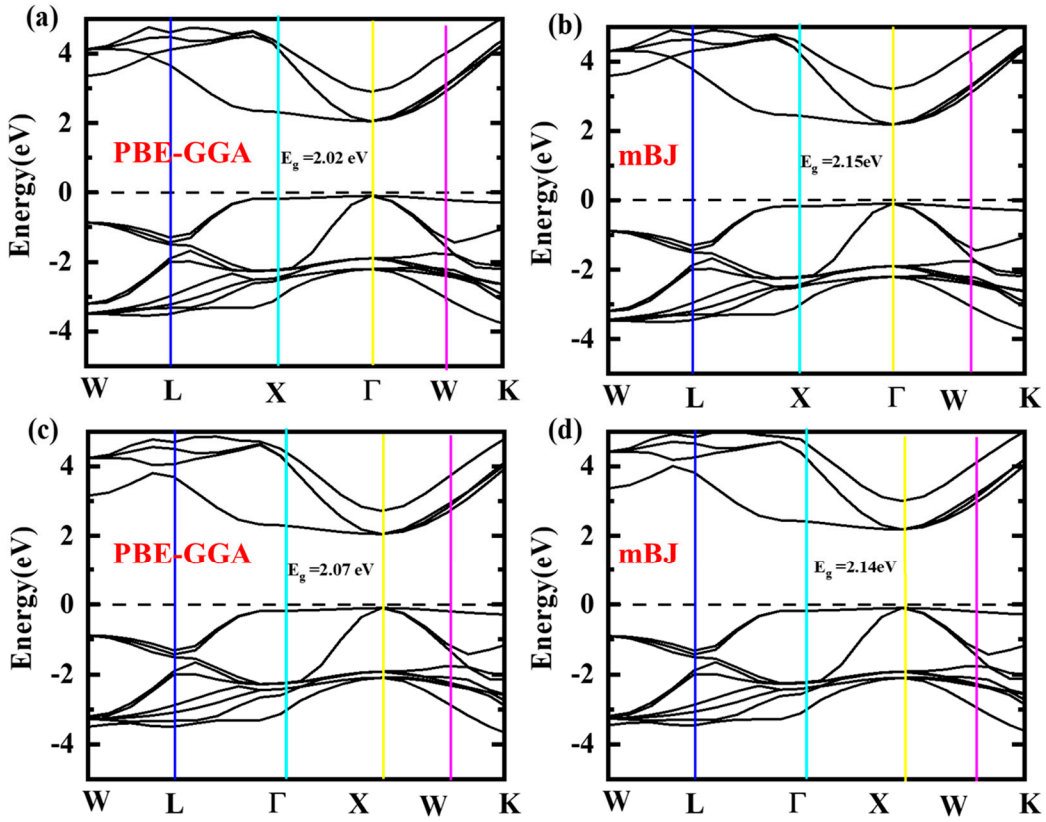

Figure 5. Computed band structure for employing GGA and mBJ for (**a**,**c**) $RbSnBr_3$ and (**b**,**d**) $CsSnBr_3$.

The elemental contribution for the studied $XSnBr_3$ (X = Rb/Cs) is advocated from the density of states plot (DOS) as represented in Figure 6a,b. The Fermi level, which is calibrated to be at 0 eV and can be shown to be near the valence band in both compounds on the band plots, suggests that the material is a p-type semiconductor. The valence band at the Fermi level is produced by the combination of the Rb/Cs and Sn states [52]. As shown in Figure 6a,b, the conduction band formed through the hybridization of Rb/Cs and Br with an Sn atom contribution. Table 3 lists the evaluated effective masses for $XSnBr_3$ (X = Rb/Cs) in the high symmetry primary directions of the Brillouin zone. Understanding the effective masses (m^*) of carriers (holes and electrons), which are greatly impacted by resistivity, carrier mobility, and optical response of free carriers, is essential for increasing photovoltaic characteristics [53]. It can be computed from band structure $E_n(k)$ as

$$\frac{1}{m^*} = \frac{1}{\hbar^2} \frac{d^2 E_n(k)}{dk^2} \tag{6}$$

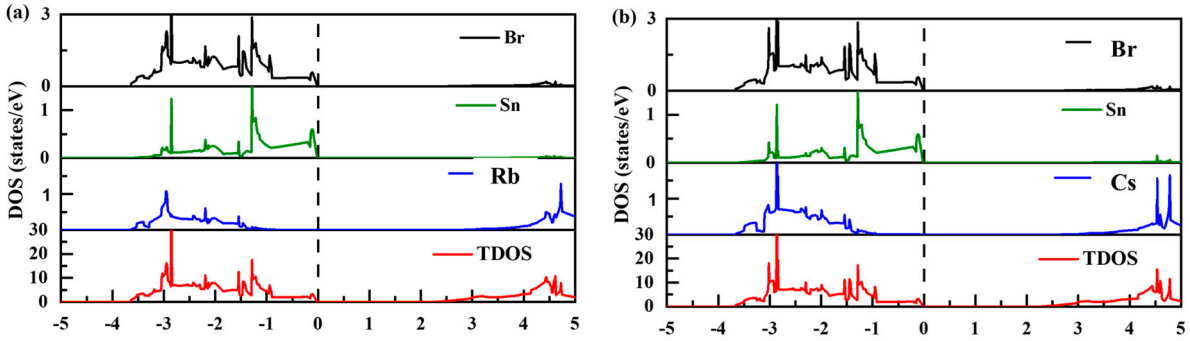

Figure 6. Computed band structure for (**a**) $RbSnBr_3$ and (**b**) $CsSnBr_3$ applying mBJ.

Table 3. Calculated bandgap utilizing various exchange correlation functional, effective mass of electrons (m_e*) and holes (m_h*), Bader charges (employing PBE-GGA methodology) XSnBr3 (X = Rb/Cs).

HHs	GGA	mBJ	Effective Mass	Bader Charge
$RbSnBr_3$	2.02	2.15	$m_e^* = 0.27$ $m_h^* = 0.29$	Rb = 0.85 Sn = 1.06 Br = −1.52
$CsSnBr_3$	2.07	2.14	$m_e^* = 0.26$ $m_h^* = 0.28$	Cs = 0.87 Sn = 1.12 Br = −1.62
Other Studies [42]		2.20		

Table 3 records the values of the projected effective mass for the $XSnBr_3$ (X = Rb/Cs) compounds under investigation. The results reveal that the compounds under research have incredibly small effective masses. A lower effective mass is highly advantageous for solar materials because it facilitates the easier transmission of carriers. This could demonstrate the effectiveness of $XSnBr_3$ (X = Rb/Cs) in photovoltaic applications.

The electron localization function (ELF) [54] for $XSnBr_3$ (X = Rb/Cs) is projected on the (110) plane, as seen in Figure 7a,b. We used the ELF to look for atom-to-atom bonds in $XSnBr_3$ (X = Rb/Cs) compounds. Figure 7a,b imply that the Rb/Cs-Sn, Sn-Br bonding are covalent. As seen in Figure 7, the electron cloud of Br is red, suggesting accepting the electrons from the other network. The Bader charge analysis depicted in Table 3 leads to additional support for this. The fact that Br can accept electrons from Rb/Cs and Sn supports the idea that it is an ion. Switching Rb to Cs has a significant effect on Bader charges, as represented in Table 3. The Bader charge increases with the increase in atomic number and probably due to the increase in states [55].

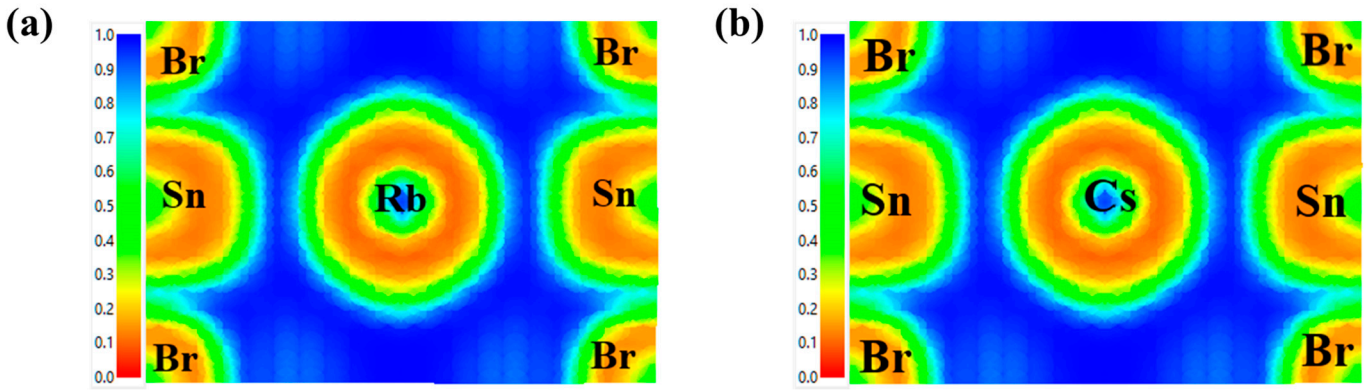

Figure 7. Electron density contour for (**a**) $RbSnBr_3$ and (**b**) $CsSnBr_3$ applying GGA.

3.4. Optical Properties

In this subsection, we highlight more details about the optical properties of the examined $XSnBr_3$ (X = Rb/Cs) compounds, inspired by their direct bandgaps and wide bandgaps. To obtain the precise knowledge needed for use in optoelectronic and photovoltaic applications, it is important to analyze the optical properties of the material [56]. The real $\varepsilon_1(\omega)$ and imaginary $\varepsilon_2(\omega)$ components of the complex dielectric function $\varepsilon(\omega)$ are considered for the computation of optical properties which are written as,

$$\varepsilon(\omega) = \varepsilon_1(\omega) + \varepsilon_2(\omega)$$

Figure 8a,b represent the variation of $\varepsilon_1(\omega)$ and $\varepsilon_2(\omega)$ with photon energy. Interaction of the light with the material results in polarization, quantified by $\varepsilon_1(\omega)$, as well as the loss of energy because of light dispersion, given by $\varepsilon_2(\omega)$. At zero energy, $\varepsilon_1(\omega)$

is quantified by $\varepsilon_1(0)$. It is noticed that with the variation of the atom Rb to Cs, $\varepsilon_1(0)$ increases with the more polarizing nature of the larger atoms, in accordance with Penn's model (i.e., $\varepsilon_1(0) = 1 + (h\omega_p/E_g)$) that is inversely linked to the bandgap [57]. After $\varepsilon_1(0)$, the graph shows the variation with the number of peaks that are commonly known as relaxation peaks. These peaks are useful in the determination of the relaxation frequency. However, due to the inverse relation between the relaxation frequency and total mass of the oscillating atoms, these peaks are observed to move towards lower energy [41]. The primary peaks in the $\varepsilon_1(\omega)$ plot are observed in the visible region. By employing the relationship $n^2(\omega) = \varepsilon_1(\omega)$, the refractive index can be computed. As observed in Figure 8c, the n (ω) plot is similar to $\varepsilon_1(\omega)$. The calculated values of n(ω) are illustrated in Table 4. Figure 8b represents the variation of $\varepsilon_2(\omega)$ with incoming radiation. The optical bandgap, as well as the absorption characteristics, are represented by $\varepsilon_2(\omega)$. It is noticed that no absorption is achieved up to 2.06 eV and 2.11 eV for $XSnBr_3$ (X = Rb/Cs) with validating the optical bandgap, which is approximately equal to the electronic bandgap. The reflectance R(ω) of the $XSnBr_3$ (X = Rb/Cs) over the energy range of 0 eV to 10 eV is exhibited in Figure 8d; $XSnBr_3$ (X = Rb/Cs) exhibits normal semiconducting properties with reflectivity less than 0.6. The measurement of reflectance at zero energy is known as absolute reflectivity, or R(0). Table 4 displays R(0)'s magnitude. After R(0), the reflectivity increases and decreases when it reaches its maximum value. The detailed investigation of optical properties reveals exceptional photoelectric capabilities, indicating enormous potential for utilization in the absorber layer of a solar cell.

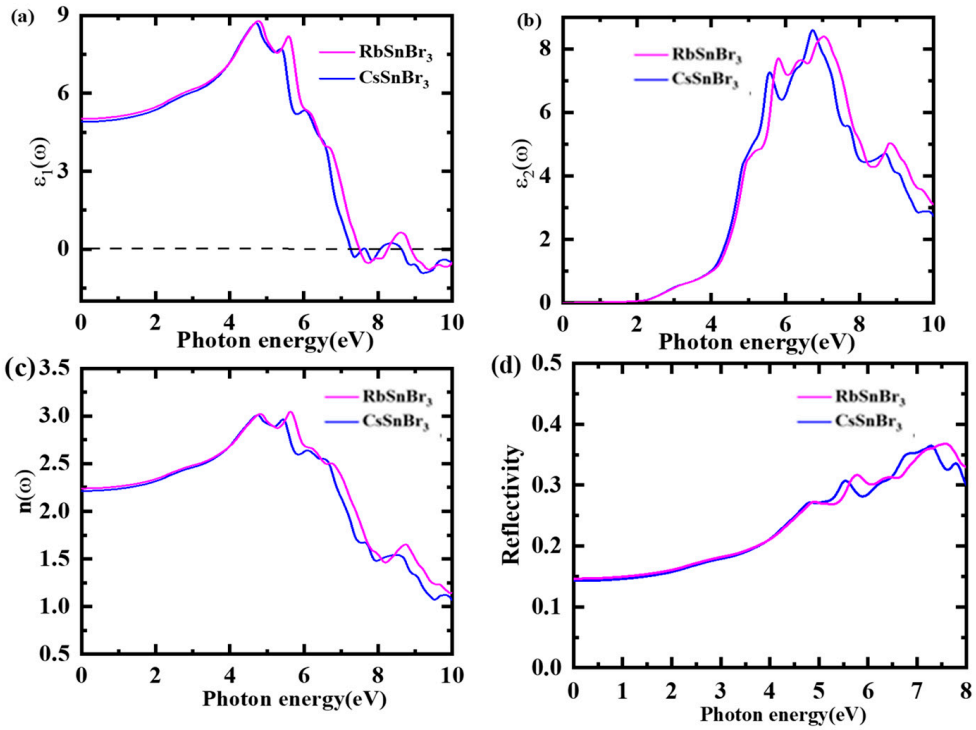

Figure 8. Computed (**a**) real part $\varepsilon_1(\omega)$, (**b**) imaginary part $\varepsilon_2(\omega)$ of dielectric, (**c**) refractive index n (ω), and (**d**) reflectivity R(ω) for $XSnBr_3$ (X = Rb/Cs).

3.5. Thermoelectricity

Semiclassical Boltzmann theory is used to examine the thermoelectric properties of the tested XSnBr3 (X = Rb/Cs) HHs while taking constant time relaxation time (τ) into consideration. The Seebeck coefficient (S), thermal conductivity (κ/τ), and electrical conductivity (σ/τ) are taken into account. The Seebeck coefficient (S) is regarded as a crucial consideration when examining thermoelectric (TE) qualities. Higher Figure of Merit (ZT) values, which indicate a material's suitability for thermoelectric applications, are preferable

to lower Seebeck values. The Seebeck coefficient (charge and heat) is related to the electron carriers. The Seebeck coefficient must be high for the thermoelectric performance to be optimum. It is positive for p-type materials but negative for n-type materials [58,59]. The investigated compound is p-type as evidenced from Figure 9a. S values for the investigated $XSnBr_3$ (X = Rb/Cs) compounds at room temperature were 249 μV/K and 298 μV/K, respectively, as indicated in Table 4. The valence electrons become less tightly bound and need less energy as the ionic scale rises from Rb to Cs. The quantity of free charge carriers increases along with electrical conductivity as well. This is due to the possibility that the potentials preserved across the sample edges may drop as the bandgap closes, and the number of free charge carriers rises at lesser exciting energies, much to how S declines as an atom moves from Rb to Cs.

Table 4. Calculated optical properties (at zero energy) and transport properties (at 300 K) for XSnBr3 (X = Rb/Cs).

	Material Property	$RbSnBr_3$	$CsSnBr_3$	Other Study [42]
Optical properties	$\varepsilon_1(0)$	5.03	4.88	5.92
	$n(0)$	2.24	3.08	2.43
Transport properties (300 K)	S(μVK)	249	298	
	$\sigma/\tau(\Omega ms)^{-1}(10^{17})$	0.61	1.1	
	k/τ (W/mKs)(1013)	0.21	0.20	
	ZT	0.79	0.83	

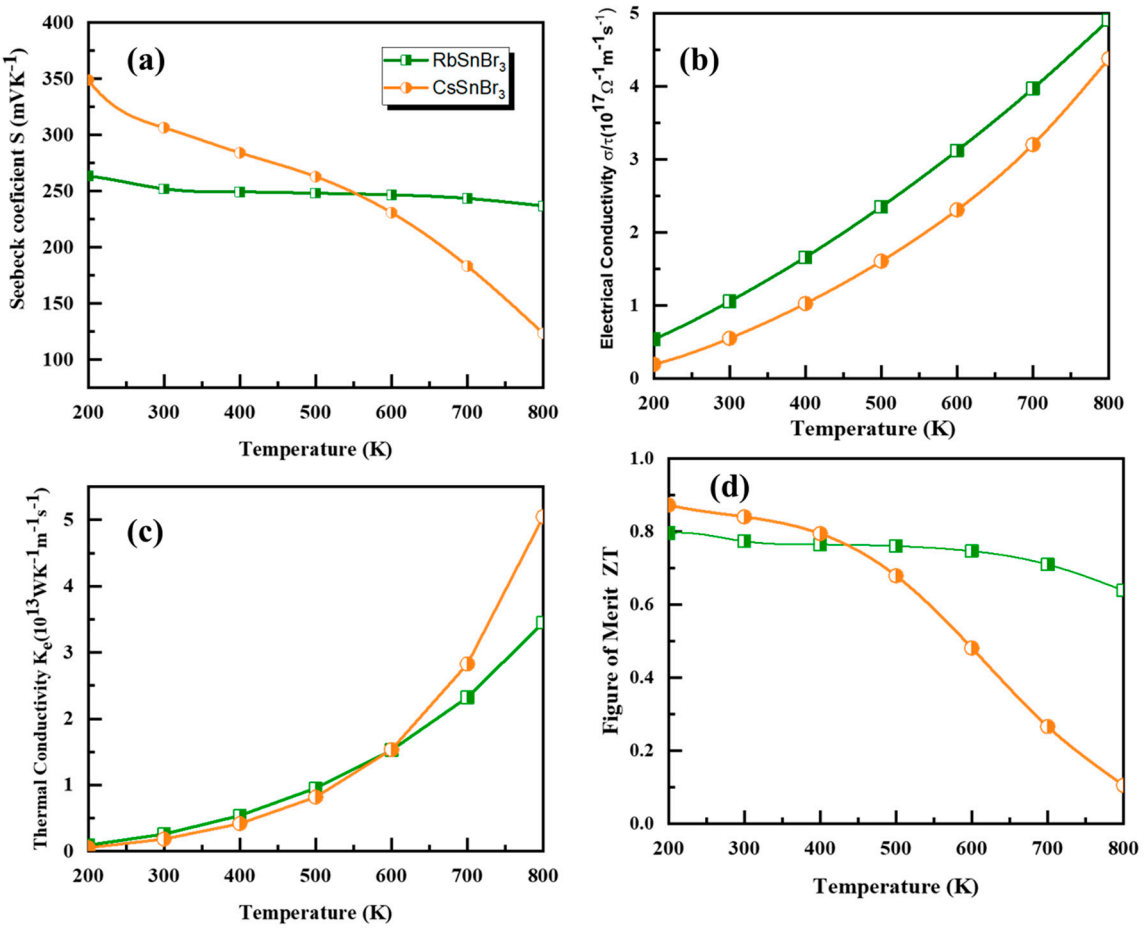

Figure 9. Calculated (**a**) Seebeck coefficient S, (**b**) electrical conductivity σ/τ, (**c**) thermal conductivity κ/τ, and (**d**) power factor S2σ/τ for XSnBr3 (X = Rb/Cs).

Furthermore, it appears that the compounds under investigation have an outstanding thermoelectric response, which is essential considering that the ideal TE material has a Seebeck value higher than 200 μV/K [45]. The computed S is bigger than earlier reporting, as seen in Table 4. Figure 9b represents the variation of electrical conductivity with temperature change. At 300 K, they are determined to be 1.1×10^{18} $\Omega m^{-1}S^{-1}$ and 0.61×10^{17} $\Omega m^{-1}S^{-1}$ for $RbSnBr_3$ and $CsSnBr_3$, respectively. An increase in σ/τ as the temperature rises is a typical pattern for semiconductor materials. The high density of charge carriers in the cubic perovskite under investigation contributes to its excellent electrical conductivity. Both electronic and lattice thermal conductivities collectively constitute the thermal lattice conductivity [60]. Lattice thermal conductivity arises from phonons, whereas electronic thermal conductivity is produced by the movements of electrons and holes. Electrical and thermal conductivity are connected according to the Wiedemann–Franz law. It was discovered to be on the order of 10^{-5}, which indicates both poor heat conductivity and strong electrical conductivity. A thermoelectric compound's efficiency can be calculated using the ZT figure of merit [8]. Figure 9d displays the computed ZT for the investigated $XSnBr_3$ (X = Rb/Cs) compounds. The estimated ZT at room temperature for $RbSnBr_3$ and $CsSnBr_3$ compounds is found to be 0.79 and 0.83, respectively. Because the compounds have a high ZT, they can be employed in thermoelectric devices. According to Table 4, the computed PF is seen to be greater than in earlier reports. The $XSnBr_3$ (X = Rb/Cs) discovered should be further investigated for its applicability in thermoelectric devices. Finally, this study sheds light on using the proposed compound in solar cells, one of the most significant renewable energy sources [61].

4. Conclusions

The structural, magnetic, electrical, elastic, vibrational, optical, thermodynamic, and thermoelectric properties of quaternary $XSnBr_3$ (X = Rb/Cs) compounds are fully investigated with the use of DFT as implemented in the Wien2k code. The calculated equilibrium structure data accord well with the majority of the related theoretical and experimental literature. The volume optimization curves show that the examined compounds are stable crystal structures. These compounds' calculated formation energy demonstrates their thermodynamic stability. The mechanical stability of $XSnBr_3$ (X = Rb/Cs) compounds is satisfied by the computed second-order elastic constants for these compounds. Additionally, the effects of incident electromagnetic radiations up to 10 eV on the fluctuation of optical characteristics including dielectric function, refractive index, reflectivity are investigated. The figure of merit (ZT) at room temperature is computed to be 0.79 and 0.83 for $XSnBr_3$ (X = Rb/Cs). As a result, $XSnBr_3$ (X = Rb/Cs) compounds have the potential to be cutting-edge and fascinating thermoelectric materials that can also be applied to optoelectronic and energy-harvesting systems.

Author Contributions: All persons who meet authorship criteria are listed as authors, and all authors certify that they have participated sufficiently in the work to take public responsibility for the content, including participation in the concept, design, analysis, writing, or revision of the manuscript. D.B., Conceptualization, Methodology, Software, Writing—Original draft preparation, Writing—Reviewing and Editing. B.A., Methodology, Software, Writing—Reviewing and Editing. S.K.M., Conceptualization, Methodology, Software, Writing—Reviewing, Validation Investigation Validation. T.A.G., Design, Analysis, Software, Writing—Reviewing and Editing. A.S., Investigation, Writing—Reviewing and Editing. M.M.S., Investigation, Writing—Reviewing and Editing, Resources. All authors have read and agreed to the published version of the manuscript.

Funding: This research received no external funding.

Data Availability Statement: The raw/processed data can be made available with a reasonable request to the corresponding author.

Conflicts of Interest: The authors declare that they have no known competing financial interests or personal relationships that could have appeared to influence the work reported in this paper.

References

1. Jarman, J.T.; Khalil, E.E.; Khalaf, E. Energy Analyses of Thermoelectric Renewable Energy Sources. *Open J. Energy Effic.* **2013**, *2013*, 143–153. [CrossRef]
2. Haq, B.U.; Ahmed, R.; AlFaify, S.; Butt, F.K.; Shaari, A.; Laref, A. Exploring Thermoelectric Materials for Renewable Energy Applications: The Case of Highly Mismatched Alloys Based on AlBi1-XSbx and InBi1-XSbx. *Intermetallics* **2018**, *93*, 235–243. [CrossRef]
3. Goldsmid, H.J. *Introduction to Thermoelectricity*; Springer: Berlin/Heidelberg, Germany, 2010; Volume 121. ISBN 3642007570.
4. Behera, D.; Al-Qaisi, S.; Manzoor, M.; Sharma, R.; Srivastava, V.; mana Al-Anazy, M.; El Shiekh, E.; Mukherjee, S.K. First Principles Studies on Optoelectronics and Transport Properties of KSrY (Y= Sb, Bi) for Renewable Energy Application. *Mater. Sci. Eng. B* **2023**, *297*, 116765. [CrossRef]
5. Dixit, A.; Saxena, A.; Sharma, R.; Behera, D.; Mukherjee, S. *Solar Photovoltaic Principles*; Ismail, B.I., Ed.; IntechOpen: Rijeka, Croatia, 2023; p. Ch. 1. ISBN 978-1-83768-677-3.
6. Goldsmid, H.J. Improving the Thermoelectric Figure of Merit. *Sci. Technol. Adv. Mater.* **2021**, *22*, 280–284. [CrossRef] [PubMed]
7. Behera, D.; Sharma, R.; Ullah, H.; Waheed, H.S.; Mukherjee, S.K. Electronic, Optical, and Thermoelectric Investigations of Zintl Phase AAg2Se2 (A= Sr, Ba) Compounds: A First First-Principles Approach. *J. Solid State Chem.* **2022**, *312*, 123259. [CrossRef]
8. Nemir, D.; Beck, J. On the Significance of the Thermoelectric Figure of Merit Z. *J. Electron. Mater.* **2010**, *39*, 1897–1901. [CrossRef]
9. Kharlamov, V.F. Thermoelectric Figure of Merit of a Material Consisting of Semiconductor or Metal Particles. *J. Exp. Theor. Phys.* **2013**, *117*, 83–88. [CrossRef]
10. Wu, T.; Gao, P. Development of Perovskite-Type Materials for Thermoelectric Application. *Materials* **2018**, *11*, 999. [CrossRef]
11. Haque, M.A.; Kee, S.; Villalva, D.R.; Ong, W.; Baran, D. Halide Perovskites: Thermal Transport and Prospects for Thermoelectricity. *Adv. Sci.* **2020**, *7*, 1903389. [CrossRef]
12. Manzoor, M.; Behera, D.; Sharma, R.; Iqbal, M.W.; Mukherjee, S.K.; Khenata, R.; Bin-Omran, S.; Alshahrani, T.; El Shiekh, E.; Ouahrani, T. Structural, Electronic, Optical, and Thermoelectric Studies on Zintl $SrCd_2Pn_2$ (Pn= P/As) Compounds for Solar Cell Applications: A First Principle Approach. *J. Solid State Chem.* **2023**, *326*, 124188. [CrossRef]
13. Kumavat, S.R.; Sonvane, Y.; Singh, D.; Gupta, S.K. Two-Dimensional $CH_3NH_3PBI_3$ with High Efficiency and Superior Carrier Mobility: A Theoretical Study. *J. Phys. Chem. C* **2019**, *123*, 5231–5239. [CrossRef]
14. Andrianov, A.V.; Aleshin, A.N.; Matyushkin, L.B. Terahertz Vibrational Modes in $CH_3NH_3PBI_3$ and $CsPbI_3$ Perovskite Films. *JETP Lett.* **2019**, *109*, 28–32. [CrossRef]
15. Afsari, M.; Boochani, A.; Shirdel, F. Electronic and Optical Properties of Two Propounded Compound in Photovoltaic Applications, CsPbI3 and CH3NH3PbI3: By DFT. *Optik* **2019**, *199*, 163360. [CrossRef]
16. Roknuzzaman, M.; Ostrikov, K.; Wang, H.; Du, A.; Tesfamichael, T. Towards Lead-Free Perovskite Photovoltaics and Optoelectronics by Ab-Initio Simulations. *Sci. Rep.* **2017**, *7*, 14025. [CrossRef]
17. Wu, Y.; Li, X.; Zeng, H. Lead-free Halide Double Perovskites: Structure, Luminescence, and Applications. *Small Struct.* **2021**, *2*, 2000071. [CrossRef]
18. Mukhtar, M.W.; Ramzan, M.; Rashid, M.; Hussain, A.; Naz, G.; Ciftci, Y.O.; Dahshan, A.; Znaidia, S. Systematic Study of Optoelectronic and Thermoelectric Properties of New Lead-Free Halide Double Perovskites A2KGaI6 (A= Cs, Rb) for Solar Cell Applications via Ab-Initio Calculations. *Mater. Sci. Eng. B* **2022**, *285*, 115957. [CrossRef]
19. Zhao, X.-G.; Yang, J.-H.; Fu, Y.; Yang, D.; Xu, Q.; Yu, L.; Wei, S.-H.; Zhang, L. Design of Lead-Free Inorganic Halide Perovskites for Solar Cells via Cation-Transmutation. *J. Am. Chem. Soc.* **2017**, *139*, 2630–2638. [CrossRef]
20. Xiao, Z.; Yan, Y. Progress in Theoretical Study of Metal Halide Perovskite Solar Cell Materials. *Adv. Energy Mater.* **2017**, *7*, 1701136. [CrossRef]
21. Li, C.; Lu, X.; Ding, W.; Feng, L.; Gao, Y.; Guo, Z. Formability of Abx3 (X= f, Cl, Br, i) Halide Perovskites. *Acta Crystallogr. Sect. B: Struct. Sci.* **2008**, *64*, 702–707. [CrossRef]
22. Sun, J.; Singh, D.J. Thermoelectric Properties of N-Type $SrTiO_3$. *APL Mater.* **2016**, *4*, 104803. [CrossRef]
23. Aboub, Z.; Seddik, T.; Daoudi, B.; Boukraa, A.; Behera, D.; Batouche, M.; Mukherjee, S.K. Impact of La, Ni-Doping on Structural and Electronic Properties of $SrTiO_3$ for Photocatalytic Water Splitting. *Inorg. Chem. Commun.* **2023**, *153*, 110871. [CrossRef]
24. Asmara, T.C.; Annadi, A.; Santoso, I.; Gogoi, P.K.; Kotlov, A.; Omer, H.M.; Motapothula, M.; Breese, M.B.H.; Rübhausen, M.; Venkatesan, T. Mechanisms of Charge Transfer and Redistribution in $LaAlO_3/SrTiO_3$ Revealed by High-Energy Optical Conductivity. *Nat. Commun.* **2014**, *5*, 3663. [CrossRef] [PubMed]
25. Bouadjemi, B.; Bentata, S.; Abbad, A.; Benstaali, W. Ab-Initio Study of Optoelectronic and Magnetic Properties of the Orthorhombic $NdMnO_3$ Perovskite. *Solid State Commun.* **2015**, *207*, 9–15. [CrossRef]
26. Murtaza, G.; Ahmad, I.; Amin, B.; Afaq, A.; Maqbool, M.; Maqssod, J.; Khan, I.; Zahid, M. Investigation of Structural and Optoelectronic Properties of $BaThO_3$. *Opt. Mater.* **2011**, *33*, 553–557. [CrossRef]
27. Noor, N.A.; Hassan, M.; Rashid, M.; Alay-e-Abbas, S.M.; Laref, A. Systematic Study of Elastic, Electronic, Optical and Thermoelectric Properties of Cubic $BiBO_3$ and $BiAlO_3$ Compounds at Different Pressure by Using Ab-Initio Calculations. *Mater. Res. Bull.* **2018**, *97*, 436–443. [CrossRef]
28. Aktary, M.; Kamruzzaman, M.; Afrose, R. A Comparative Study of the Mechanical Stability, Electronic, Optical and Photocatalytic Properties of CsPbX 3 (X= Cl, Br, I) by DFT Calculations for Optoelectronic Applications. *RSC Adv.* **2022**, *12*, 23704–23717. [CrossRef]

29. Sabir, B.; Murtaza, G.; Khalil, R.M.A.; Mahmood, Q. First Principle Study of Electronic, Mechanical, Optical and Thermoelectric Properties of CsMO3 (M= Ta, Nb) Compounds for Optoelectronic Devices. *J. Mol. Graph. Model.* **2019**, *86*, 19–26. [CrossRef]
30. Ilyas, A.; Khan, S.A.; Liaqat, K.; Usman, T. Investigation of the Structural, Electronic, Magnetic, and Optical Properties of $CsXO_3$ (X= Ge, Sn, Pb) Perovskites: A First-Principles Calculations. *Optik* **2021**, *244*, 167536. [CrossRef]
31. Blaha, P.; Schwarz, K.; Sorantin, P.; Trickey, S.B. Full-Potential, Linearized Augmented Plane Wave Programs for Crystalline Systems. *Comput. Phys. Commun.* **1990**, *59*, 399–415. [CrossRef]
32. Blaha, P.; Schwarz, K.; Madsen, G.K.H.; Kvasnicka, D.; Luitz, J. Wien2k. *Augment. Plane Wave+ Local Orbitals Program Calc. Cryst. Prop.* **2001**, *60*, 1.
33. Perdew, J.P.; Burke, K.; Ernzerhof, M. Generalized Gradient Approximation Made Simple. *Phys. Rev. Lett.* **1996**, *77*, 3865. [CrossRef] [PubMed]
34. Koller, D.; Tran, F.; Blaha, P. Merits and Limits of the Modified Becke-Johnson Exchange Potential. *Phys. Rev. B* **2011**, *83*, 195134. [CrossRef]
35. Behera, D.; Manzoor, M.; Maharana, M.; Iqbal, M.W.; Zahid, T.; Lakra, S.; Mukherjee, S.K.; Alarfaji, S.S. Structural, Electronic, Optical, and Thermoelectric Response of Zintl Phase AAg2S2 (A= Sr/Ba) Compounds for Renewable Energy Applications. *Phys. B Condens. Matter* **2023**, *649*, 414446. [CrossRef]
36. Madsen, G.K.H.; Singh, D.J. BoltzTraP. A Code for Calculating Band-Structure Dependent Quantities. *Comput. Phys. Commun.* **2006**, *175*, 67–71. [CrossRef]
37. Sharma, R.; Dey, A.; Dar, S.A.; Srivastava, V. A DFT Investigation of CsMgX3 (X= Cl, Br) Halide Perovskites: Electronic, Thermoelectric and Optical Properties. *Comput. Theor. Chem.* **2021**, *1204*, 113415. [CrossRef]
38. Katsura, T.; Tange, Y. A Simple Derivation of the Birch–Murnaghan Equations of State (EOSs) and Comparison with EOSs Derived from Other Definitions of Finite Strain. *Minerals* **2019**, *9*, 745. [CrossRef]
39. Fedorovskiy, A.E.; Drigo, N.A.; Nazeeruddin, M.K. The Role of Goldschmidt's Tolerance Factor in the Formation of A2BX6 Double Halide Perovskites and Its Optimal Range. *Small Methods* **2020**, *4*, 1900426. [CrossRef]
40. Emery, A.A.; Wolverton, C. High-Throughput DFT Calculations of Formation Energy, Stability and Oxygen Vacancy Formation Energy of ABO3 Perovskites. *Sci. Data* **2017**, *4*, 170153. [CrossRef]
41. Behera, D.; Mukherjee, S.K. Optoelectronics and Transport Phenomena in Rb2InBiX6 (X= Cl, Br) Compounds for Renewable Energy Applications: A DFT Insight. *Chemistry* **2022**, *4*, 1044–1059. [CrossRef]
42. Mahmood, Q.; Yaseen, M.; Hassan, M.; Rashid, M.S.; Tlili, I.; Laref, A. The First-Principle Study of Mechanical, Optoelectronic and Thermoelectric Properties of $CsGeBr_3$ and $CsSnBr_3$ Perovskites. *Mater. Res. Express* **2019**, *6*, 45901. [CrossRef]
43. Anderson, O.; Schreiber, E.; Soga, N. *Elastic Constants and Their Measurements*; McGraw-Hill Companies, Inc.: New York, NY, USA, 1973.
44. Mouhat, F.; Coudert, F.-X. Necessary and Sufficient Elastic Stability Conditions in Various Crystal Systems. *Phys. Rev. B* **2014**, *90*, 224104. [CrossRef]
45. Behera, D.; Mukherjee, S.K. Theoretical Investigation of the Lead-Free K_2InBiX_6 (X= Cl, Br) Double Perovskite Compounds Using First Principle Calculation. *JETP Lett.* **2022**, *116*, 537–546. [CrossRef]
46. Behera, D.; Dixit, A.; Nahak, B.; Srivastava, A.; Dubey, S.; Sharma, R.; Mishra, A.K.; Mukherjee, S.K. Structural, Electronic, Elastic, Vibrational and Thermodynamic Properties of Antiperovskites Mg_3NX (X= Ge, Sn): A DFT Study. *Phys. Lett. A* **2022**, *453*, 128478. [CrossRef]
47. Al-Qaisi, S.; Rached, H.; Alrebdi, T.A.; Bouzgarrou, S.; Behera, D.; Mukherjee, S.K.; Khuili, M.; Adam, M.; Verma, A.S.; Ezzeldien, M. Study of Mechanical, Optical, and Thermoelectric Characteristics of Ba_2XMoO_6 (X= Zn, Cd) Double Perovskite for Energy Harvesting. *J. Comput. Chem.* **2023**. [CrossRef]
48. Kube, C.M. Elastic Anisotropy of Crystals. *AIP Adv.* **2016**, *6*, 95209. [CrossRef]
49. Chung, D.H.; Buessem, W.R. The Elastic Anisotropy of Crystals. *J. Appl. Phys.* **1967**, *38*, 2010–2012. [CrossRef]
50. Pugh, S.F. XCII. Relations between the Elastic Moduli and the Plastic Properties of Polycrystalline Pure Metals. *Lond. Edinb. Dublin Philos. Mag. J. Sci.* **1954**, *45*, 823–843. [CrossRef]
51. Dixit, A.; Behera, D.; Tripathi, S.K.; Srivastava, A.; Sharma, R.; Khenata, R.; Albalawi, H.; Mahmoud, Z.; Mukherjee, S.K. Vibrational, Mechanical, Electronic and Thermodynamic Properties of Rhenium-Based Perovskites $XReO_3$ (X= Li, Be) by an Ab-Initio Computation. *Mater. Sci. Eng. B* **2023**, *294*, 116545. [CrossRef]
52. Behera, D.; Manzoor, M.; Iqbal, M.W.; Lakra, S.; Mukherjee, S.K. Revealing Excellent Electronic, Optical, and Thermoelectric Behavior of EU Based $Euag_2y_2$ (Y= S/Se): For Solar Cell Applications. *Comput. Condens. Matter* **2022**, *32*, e00723. [CrossRef]
53. Cohen, M.H.; Ham, F.S. Electron Effective Mass in Solids—A Generalization of Bardeen's Formula. *J. Phys. Chem. Solids* **1960**, *16*, 177–183. [CrossRef]
54. Savin, A.; Nesper, R.; Wengert, S.; Fässler, T.F. ELF: The Electron Localization Function. *Angew. Chem. Int. Ed. Engl.* **1997**, *36*, 1808–1832. [CrossRef]
55. Watcharatharapong, T.; Minakshi Sundaram, M.; Chakraborty, S.; Li, D.; Shafiullah, G.M.; Aughterson, R.D.; Ahuja, R. Effect of Transition Metal Cations on Stability Enhancement for Molybdate-Based Hybrid Supercapacitor. *ACS Appl. Mater. Interfaces* **2017**, *9*, 17977–17991. [CrossRef] [PubMed]
56. Abt, R.; Ambrosch-Draxl, C.; Knoll, P. Optical Response of High Temperature Superconductors by Full Potential LAPW Band Structure Calculations. *Phys. B: Condens. Matter* **1994**, *194*, 1451–1452. [CrossRef]
57. Penn, D.R. Wave-Number-Dependent Dielectric Function of Semiconductors. *Phys. Rev.* **1962**, *128*, 2093. [CrossRef]

58. Cai, J.; Mahan, G.D. Effective Seebeck Coefficient for Semiconductors. *Phys. Rev. B* **2006**, *74*, 75201. [CrossRef]
59. Behera, D.; Mohammed, B.; Taieb, S.; Mokhtar, B.; Al-Qaisi, S.; Mukherjee, S.K. First-Principle Investigations on Optoelectronics and Thermoelectric Properties of Lead-Free Rb_2InSbX_6 (X= Cl, Br) Double Perovskites: For Renewable Energy Applications. *Eur. Phys. J. Plus* **2023**, *138*, 520. [CrossRef]
60. Haque, E.; Hossain, M.A. Origin of Ultra-Low Lattice Thermal Conductivity in Cs2BiAgX6 (X= Cl, Br) and Its Impact on Thermoelectric Performance. *J. Alloys Compd.* **2018**, *748*, 63–72. [CrossRef]
61. Shaheen, M.A.M.; Hasanien, H.M.; Turky, R.A.; Ćalasan, M.; Zobaa, A.F.; Abdel Aleem, S.H.E. OPF of Modern Power Systems Comprising Renewable Energy Sources Using Improved CHGS Optimization Algorithm. *Energies* **2021**, *14*, 6962. [CrossRef]